Chemical Science

ROYAL SOCIETY OF CHEMISTRY

EDGE ARTICLE

View Article Online
View Journal | View Issue

Cite this: *Chem. Sci.*, 2021, **12**, 12383

All publication charges for this article have been paid for by the Royal Society of Chemistry

A vanadium-based oxide-phosphate-pyrophosphate framework as a 4 V electrode material for K-ion batteries†

Mirai Ohara,[a] A. Shahul Hameed,[ab] Kei Kubota,[ab] Akihiro Katogi,[a] Kuniko Chihara,[ab] Tomooki Hosaka[ab] and Shinichi Komaba *[ab]

Received 8th July 2021
Accepted 12th August 2021

DOI: 10.1039/d1sc03725k

rsc.li/chemical-science

K-ion batteries (KIBs) are promising for large-scale electrical energy storage owing to the abundant resources and the electrochemical specificity of potassium. Among the positive electrode materials for KIBs, vanadium-based polyanionic materials are interesting because of their high working voltage and good structural stability which dictates the cycle life. In this study, a potassium vanadium oxide phosphate, $K_6(VO)_2(V_2O_3)_2(PO_4)_4(P_2O_7)$, has been investigated as a 4 V class positive electrode material for non-aqueous KIBs. The material is synthesized through pyrolysis of a single metal–organic molecular precursor, $K_2[(VOHPO_4)_2(C_2O_4)]$ at 500 °C in air. The material demonstrates a reversible extraction/insertion of 2.7 mol of potassium from/into the structure at a discharge voltage of ~4.03 V *vs.* K. *Operando* and *ex situ* powder X-ray diffraction analyses reveal that the material undergoes reversible K extraction/insertion during charge/discharge *via* a two-phase reaction mechanism. Despite the extraction/insertion of large potassium ions, the material demonstrates an insignificant volume change of ~1.2% during charge/discharge resulting in excellent cycling stability without capacity degradation over 100 cycles in a highly concentrated electrolyte cell. Robustness of the polyanionic framework is proved from identical XRD patterns of the pristine and cycled electrodes (after 100 cycles).

Introduction

Li-ion batteries (LIBs) play a significant role as power sources for portable electronics and electric vehicles (EVs) owing to their high energy densities and environmental friendliness.[1,2] In addition, the application of LIBs is now expanding exponentially to stationary electrical energy storage (EES) to harness the renewable energy sources such as solar and wind.[3] However, such large-scale energy storage employing LIBs would cause a supply-demand mismatch of lithium.[4] Owing to the global uniform distribution of sodium and potassium resources and their high abundance in the Earth's crust, the research and development of Na-ion batteries (NIBs) and K-ion batteries (KIBs) have increased significantly in recent years.[5–8] Among these two promising technologies, KIBs offer an unique advantage of high operation voltages which are comparable to that of LIBs since the redox potential of K^+/K is ~0.1 V lower than that of Li^+/Li in carbonate ester electrolyte solutions.[9] Moreover, weaker Lewis acidity of K^+ ions enables their facile diffusion in the electrolyte, enabling high-power operation.[6,7]

Since reversible electrochemical intercalation of potassium ion into graphite and its reversible capacity close to the theoretical capacity of 279 mA h g^{-1} at a potential of ~0.2 V *vs.* K^+/K with high rate capability and long cycle life have been reported in 2015,[9–11] various carbonaceous materials such as graphitizable and non-graphitizable carbons have been studied to undergo reversible K-insertion with high capacities.[12–14] Compared to the progress on negative electrode materials, the development of positive electrode materials is still in its infancy. In the case of LIBs, layered transition metal oxides are used as commercial positive electrode materials owing to their high energy densities.[15] Similarly, the Na analogues (Na_xMeO_2; where Me = transition metals and $x \leq 1$) are considered candidates for commercialization of NIBs.[16] However, in the case of potassium storage, the transition metal oxides deliver unsatisfactory capacities at lower operating potentials compared to their Li/Na counterparts.[7] Therefore, the focus is on polyanionic compounds which adopt open framework structures containing large channels and facilitate diffusion of large K^+ ions.[17–19] High energy density and long cycle life have been demonstrated in materials such as, $KTiOPO_4$-type $KVOPO_4$,[20] $KVPO_4F$,[20–22] $KFeSO_4F$,[23] and $KTiPO_4F$,[24] layered $VOPO_4$ (ref. 25) and $KVPO_4F$,[26] $KFe(SO_4)_2$,[27] $K_2[(VOHPO_4)_2(C_2O_4)]$,[28] and Prussian blue analogues such as $K_2Me[Fe(CN)_6]$.[29–35] Additionally, the redox potentials of the transition metals in the polyanionic frameworks are enhanced by the

[a]*Department of Applied Chemistry, Tokyo University of Science, 1-3 Kagurazaka, Shinjuku-ku, Tokyo 162-8601, Japan. E-mail: komaba@rs.tus.ac.jp*

[b]*ESICB, Kyoto University, 1-30 Goryo-Ohara, Nishikyo-ku, Kyoto 615-8245, Japan*

† Electronic supplementary information (ESI) available. See DOI: 10.1039/d1sc03725k

inductive effect of the strongly electronegative ligands.[36] In this context, mixed phosphate-pyrophosphate class of materials is significant as positive electrode materials for secondary batteries. For example, the average discharge voltage of a mixed phosphate-pyrophosphate material, $Na_4Fe_3(PO_4)(P_2O_7)$, is ~3.4 V, higher than the pure phosphate, $NaFePO_4$.[37] Likewise, a lithium containing hybrid material, $Li_9V_3(P_2O_7)_3(PO_4)_2$, exhibits high operating potentials with plateaus at 3.85 and 4.5 V in Li cells.[38]

Recently, our group[39] and Tereshchenko *et al.*[40] reported a potassium vanadium oxide-phosphate-pyrophosphate hybrid material, $K_6(VO)_2(V_2O_3)_2(PO_4)_4(P_2O_7)$ as a positive electrode for KIBs. The material demonstrated a capacity of 30 mA h g^{-1} at C/20 rate with unsatisfactory cycling life.[40] In this study, we have synthesized potassium vanadium (+IV and +V) oxide phosphate, $K_6(VO)_2(V_2O_3)_2(PO_4)_4(P_2O_7)$ (hereafter denoted as KVPP) *via* a different approach, a single step thermal decomposition route using a single molecular precursor, $K_2[(VOHPO_4)_2(C_2O_4)]$. The precursor, which could be obtained on a large scale by a room temperature precipitation synthesis, was decomposed at 500 °C, yielding the KVPP material. The material demonstrated a reversible capacity of 59 mA h g^{-1} with a discharge plateau of 4.03 V in 1 mol dm^{-3} KPF_6 EC/PC electrolyte. The material also demonstrated good cycling stability of ~100% when a highly concentrated electrolyte of 5.6 mol kg^{-1} of potassium bis(-fluorosulfonyl)amide (KFSA) in triethylene glycol dimethyl ether (triglyme, 3 G) was employed.

Experimental

Synthesis

Firstly, the precursor, an oxalatophosphate open framework material, $K_2[(VOHPO_4)_2(C_2O_4)]\cdot 4.5H_2O$, was obtained by a simple room temperature precipitation synthesis.[28,41] In a typical reaction, 10 mmol of V_2O_5, 14 mmol of tartaric acid and 40 mmol KOH were dissolved together in 50 mL of distilled water and 100 mmol of H_3PO_4 was added with constant stirring. After stirring for 12 h at room temperature, a greenish precipitate of $K_2[(VOHPO_4)_2(C_2O_4)]\cdot 4.5H_2O$ was resulted. It was then filtered, washed with distilled water, and then dried at 120 °C under vacuum. After calcination of the oxalatophosphate precursor at 500 °C for 5 h in air, dark-green powder of KVPP was resulted. In order to reduce the particle size, the resultant KVPP was ball-milled with acetylene black for 3 h and reheated at 500 °C in air. Since the carbon was added to maintain the oxidation state of the vanadium during calcination in air, it was pyrolyzed in air and its content in the reheated sample was found to be negligible at 0.13 mass% from elemental analysis.

Characterization

Structure of the obtained samples was characterized by X-ray diffraction (XRD) with Cu-Kα radiation (Rigaku, SmartLab). For XRD measures, we used a homemade air-tight sample holder to avoid the sample from being exposed to air. Synchrotron X-ray diffraction measurement was conducted at BL02B2 beamline[42] in SPring-8 for investigating the structure evolution during charge and discharge processes. Samples were ground and filled into a glass capillary with a diameter of 0.5 mm and sealed with a resin in an argon-filled glove box to prevent the exposure of cycled electrodes to moisture. Rietveld refinement was performed using RIETAN-FP program.[43] Schematic illustrations of the crystal structures were prepared using VESTA program.[44] Bond valance sum (BVS) of elements was also calculated using this program. Elemental analysis was carried out using a CHNS elemental analyzer (vario EL cube, Elementar). Scanning electron microscope (SEM, JCM-6000, JEOL Ltd) and transmission electron microscope (TEM, JEM-2100F, JEOL Ltd) were employed to characterize the morphology of the synthesized powder. Selected-area electron diffraction (SAED) patterns were also collected by the TEM and were simulated using SingleCrystal™: a single-crystal diffraction program (CrystalMaker Software Ltd, Oxford, England). X-ray absorption spectroscopy (XAS) was conducted at beamline BL-12C of the Photon Factory Synchrotron Source in Japan. For the XAS measurements, the cycled electrodes were sealed in a water-resistant polymer film inside an Ar-filled glove box to minimize the exposure of electrodes to moisture. XAS spectra were collected with a silicon monochromator in transmission mode. Intensities of the incident and transmitted X-rays were measured using an ionization chamber at room temperature. Analysis of the XAS spectra was carried out using the ATHENA software package based on IFEFFIT.[45]

For the electrochemical studies, a slurry containing the active material, acetylene black and poly(vinylidene fluoride) binder was mixed at a weight ratio of 7 : 2 : 1 with *N*-methylpyrrolidone, and the slurry mixture was coated onto an Al foil as a current collector and dried at 100 °C under vacuum. The electrochemical properties of KVPP were examined in coin cells with 1.0 mol dm^{-3} KPF_6 in EC : PC (1 : 1 v/v) electrolyte (Kishida Chemical Co., Ltd) and metallic potassium as a counter electrode. Li and Na half-cells were also fabricated using 1 mol dm^{-3} $LiPF_6$ in EC : DMC (1 : 1 v/v) and 1 mol dm^{-3} $NaPF_6$ in EC : PC (1 : 1 v/v) electrolytes, respectively. Charge/discharge tests of the cells were carried out in galvanostatic mode at room temperature. *Operando* XRD measurements were performed using an *in situ* three-electrode XRD cell (EC-FRONTIER) with a beryllium X-ray window using K metal as counter and reference electrodes. Pretreatment of the reference electrode was conducted to obtain a stable potential.[46] *Operando* XRD patterns were recorded on a Rigaku MultiFlex X-ray diffractometer during the first and second galvanostatic charge–discharge cycles at a slow current rate of C/40 (1C = 88 mA g^{-1}).

Results and discussion

Structure and morphology

In earlier reports of KVPP, two-step calcination routes were used for its synthesis and considerable amounts of $K_2VOP_2O_7$ was found as impurities.[40,47] In this study, the KVPP powder was successfully obtained by a simple one-step decomposition reaction using the oxalatophosphate precursor. Using a single source precursor ensures a homogeneous distribution of the elements on an atomic level and hence higher purity can be

achieved. In addition, the method helps in a faster reaction rate and a lower synthesis temperature.[48]

A synchrotron XRD pattern of the synthesized sample and its Rietveld refinement pattern are shown in Fig. 1a. Main diffraction peaks can be indexed as $K_6(VO)_2(V_2O_3)_2(PO_4)_4(P_2O_7)$ phase with a orthorhombic space group of *Pnma*, similar to the reported structure of KVPP.[47,49] In addition to the main KVPP phase, $K_2VOP_2O_7$ phase was detected as an impurity phase as shown in Fig. 1a and also found in the literatures.[40,47] The phase fraction of $K_2VOP_2O_7$ calculated from the Rietveld refinement was 2.8 mass% in the current study, which was smaller than 8.9 mass% in the literature.[40] The current synthesis method through calcination of the oxalatophosphate precursor results in the highly pure KVPP sample. Refined lattice parameters of KVPP were $a = 6.97269(6)$ Å, $b = 13.39710(10)$ Å, and $c = 14.23770(11)$ Å which are close to the previous reports.[40,47] Details of the refined structural parameters are given in Table S1.† Fig. 1b and c illustrate the crystal structure of KVPP viewed along *a*-axis and *b*-axis, respectively. The structure of KVPP[49] is known to be isostructural to $Rb_6V_6P_6O_{31}$ (or $Rb_6(VO)_2(V_2O_3)_2(PO_4)_4(P_2O_7)$).[50] The host framework $[V_6P_6O_{31}]_\infty$ consists of corner-sharing VO_6 octahedra (corresponding to V_2O_6 in Fig. 1a and b and Table S1†), corner-sharing VO_5 square pyramids to form V_2O_9 pyramidal dimer ($V1_2O_9$), and phosphate PO_4 ($P1O_4$) and pyrophosphate P_2O_7 ($P_2P_3O_7$) groups. However, the distance between the vanadium atom in the V_2O_9 pyramidal dimer and the oxygen atom in the PO_4 tetrahedra is 2.658(6) Å, which is a relatively short distance (see the length of (V1)–(O9) bond in Table S2†). Therefore, these may be described as V_2O_{10} octahedral dimer consisting of corner-sharing VO_6 octahedra, although the vanadium atoms are out of the central position of the VO_6 octahedra. The V_2O_9 (or V_2O_{10}) dimers are corner-shared with P_2O_7 units and linked with corner-sharing VO_6 octahedral chains along *b*-axis through corner-sharing PO_4 units to form the 3D framework containing tunnels along the *a*-axis which accommodate diffusible large potassium ions.

It should be noted that P_2O_7 units are arranged in disorder in the current structural model, and the P and O sites are each divided into two sites (*e.g.*, P2 and P3 in Fig. 1). In contrast, Leclaire *et al.* proposed an ordered superlattice model.[47] Thus, based on the Leclaire's supercell model with a space group of $P\bar{1}$, we considered a new $\sqrt{2} \times \sqrt{2}$ supercell model with $P2_1/c$ as well as two sub-cells with $P2_1/m$ and $Pmn2_1$ as shown in Fig. S1.† The latter two sub-cells may be the same as those recently reported by Tereshchenko.[40] The Rietveld analysis using the models, however, showed very small differences in the *R* factors from the conventional sub-cell model (Fig. S2†). Consequently, ordering sequence of P_2O_7 units was difficult to be confirmed from our synchrotron XRD data and structural refinements. Regardless of the ordering or disordering of P_2O_7 units, the potassium occupancy factors calculated from the Rietveld refinement are 0.980(2) and 0.989(2) for the K1 and K2 sites, respectively, which are close to the full occupancy. Furthermore, BVS of vanadium ions was calculated to be 4.27 for V1 of the $V1O_5$ square pyramid and 4.15 for V2 of the $V2O_6$ octahedron, indicating slightly higher oxidation state for V1.

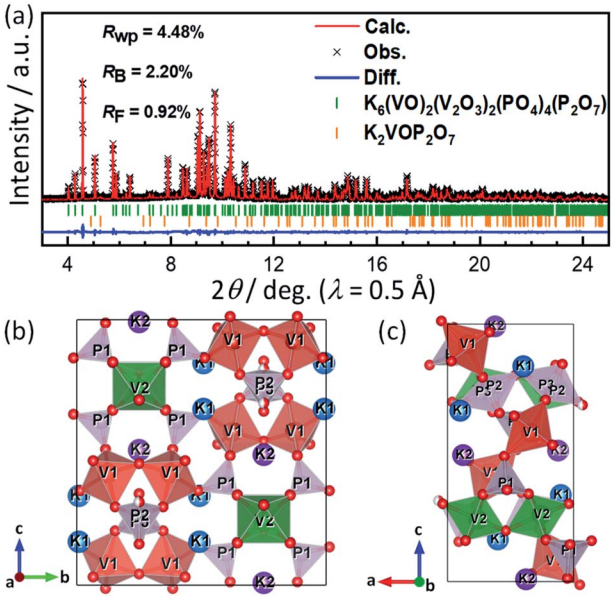

Fig. 1 (a) Rietveld refinement results on the synchrotron XRD pattern of KVPP powder sample. Black cross-marks represent the experimental pattern while the calculated pattern is shown as red lines. The blue line represents the difference between the calculated and observed patterns. The vertical bars correspond to the positions of Bragg reflections. Schematic illustrations of the refined crystal structures for $K_6(VO)_2(V_2O_3)_2(PO_4)_4(P_2O_7)$ projected along (b) *a*-axis and (c) *b*-axis.

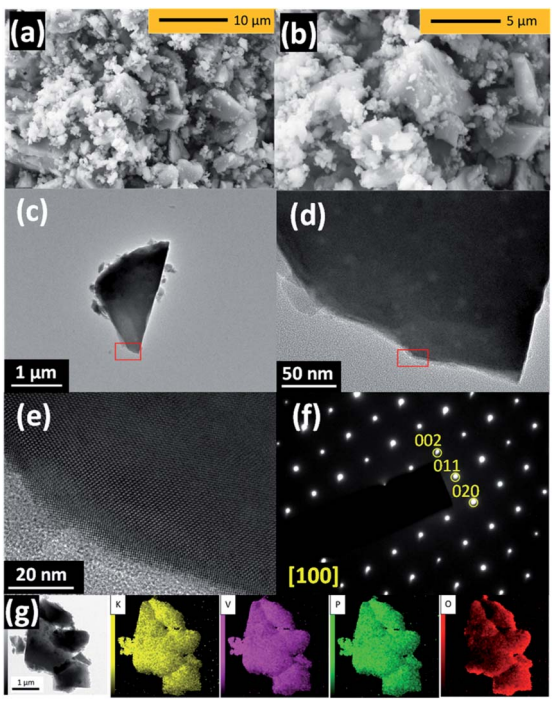

Fig. 2 (a and b) SEM and (c–e) TEM images, (f) SAED pattern, and (g) TEM-EDX mapping of as-prepared $K_6(VO)_2(V_2O_3)_2(PO_4)_4(P_2O_7)$. (b) Magnified SEM image of the panel 'a'. (d) and (e) Magnified TEM images of the red square area represented in the panel 'c' and 'd', respectively.

The morphology of KVPP was examined using SEM and TEM. From the SEM micrographs (Fig. 2a and b), it is inferred that the material contains particles of varying size ranging from few hundred nm to ~5 μm. The TEM images shown in Fig. 2c and d indicate the agglomeration of particles. A single-crystalline domain is shown in Fig. 2e and a SAED pattern of the region along the [100] zone axis is shown in Fig. 2f. The diffraction spots indexed to 002, 011, and 020 are confirmed based on the refined conventional structural model having disordered P_2O_7 units. Although the simulation pattern of the ordered sub-cell with $Pmn2_1$ agreed well with the observed SAED pattern (Fig. S3†), the determination of symmetry was difficult due to structural defects and overlap of differently oriented domains. The TEM-EDX mapping of the KVPP (Fig. 2g) proves a uniform distribution of the individual elements. The TEM-EDX spectrum shown in Fig. S4† confirms a near stoichiometric composition.

Electrochemical K-extraction/insertion

For the synthesized KVPP sample, charge–discharge tests were carried out using 1 mol dm^{-3} KPF_6 in EC : PC (= 1 : 1 v/v) as electrolyte in a K metal half-cell. Fig. 3a shows the voltage profiles of KVPP electrode at room temperature at a current rate of C/20 (1C = 88 mA g^{-1}) in the voltage window of 2.0–4.5 V *vs.* K. A constant voltage mode was employed at the end of charge and the cell voltage was held at *ca.* 4.5 V for 5 hours. The initial discharge capacity was 59 mA h g^{-1} which is ~67% of its theoretical capacity. This indicates extraction of ~2.7 mol K from the structure during the initial charge process and reversal K insertion into the framework. The voltage profiles (Fig. 3a) and the dQ/dV plot for the 2nd cycle (Fig. 3b) indicate a single redox voltage plateau at 4.18/4.03 V. The high working voltage of KVPP is due to the inductive effects of strongly electronegative PO_4 and P_2O_7 units[36] on the vanadium ions. Interestingly, the redox potential of KVPP is similar to that of $KVOPO_4$ as shown in Fig. S5.† KVPP demonstrated good cyclability in the voltage window of 2.0–4.5 V as shown in Fig. 3c and retained ~84% of the initial capacity at 100th cycle. The rate performance of the material was examined at different discharging rates and a constant charging rate of C/20, and the voltage profiles (discharge curves) at these rates are shown in Fig. 3d. With increasing current rates, the capacity of the material decreases and demonstrated a discharge capacity of 35 mA h g^{-1} at 1C rate.

To understand the origin of capacity fading during cycling, *ex situ* XRD was carried out after 100 cycles at the discharged state (2.0 V). As shown in the Fig. 4, the XRD pattern of the KVPP electrode after cycling confirmed a quite similar pattern to the pristine state. This indicates the robustness of the structure despite the extraction/insertion of large K-ions. Therefore, the slight capacity decay observed during the cycling may be attributed to electrolyte decomposition at high voltage and/or side reactions of a K metal counter electrode with the electrolyte, leading to increase of reaction resistance. Accordingly, the material was subjected to galvanostatic cycling in a highly concentrated electrolyte, 5.6 mol kg^{-1} KFSA in triglyme (G3). Highly concentrated electrolytes improve the cycling stability and coulombic efficiency of electrode materials owing to the high oxidation resistant properties and by promoting a stable SEI formation on negative electrodes.[51–56] As shown in Fig. 5b and c, the capacity retention has been improved employing the 5.6 mol kg^{-1} KFSA electrolyte. No capacity degradation was observed over 100 cycles for the 5.6 mol kg^{-1} KFSA/G3 electrolyte while the capacity retention rate was only 84% when 1 mol dm^{-3} KPF_6/EC:PC electrolyte was used.

In addition to the K system, Li- and Na-insertion properties of the KVPP framework were also investigated using Li//KVPP and Na//KVPP half-cells. Fig. S6† shows voltage profiles of these half cells cycled at C/20. The first charge process comprises the K extraction, resulting in the formation of $K_x(VO)_2(V_2O_3)_2(PO_4)_4(P_2O_7)$ where $x \approx 3.6$ based on the current passed through the cell. The differential capacity plots (dQ/dV) of the 2nd cycle for Li, Na, and K insertion into the framework are compared in Fig. S7,†

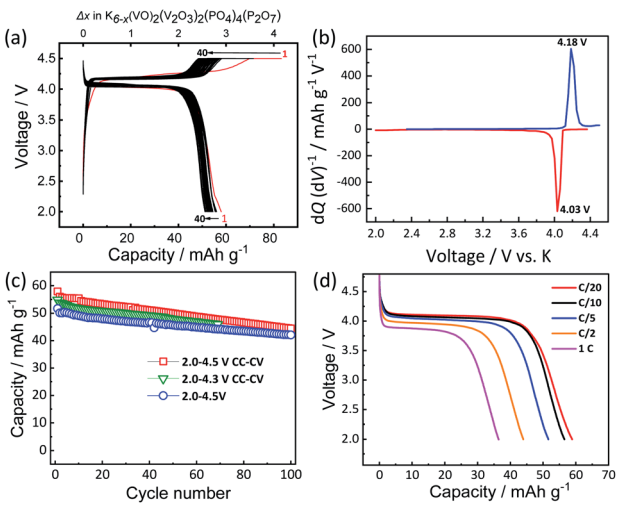

Fig. 3 Electrochemical properties of KVPP: (a) charge–discharge profiles for the first 40 cycles at C/20 current rate in the potential range of 2.0–4.5 V (with constant voltage step at 4.5 V), (b) dQ/dV plot of the second charge–discharge profile, (c) capacity retention plots of KVPP at C/20 rate in different voltage windows and (d) discharge profiles of KVPP at different current rates on the discharging process.

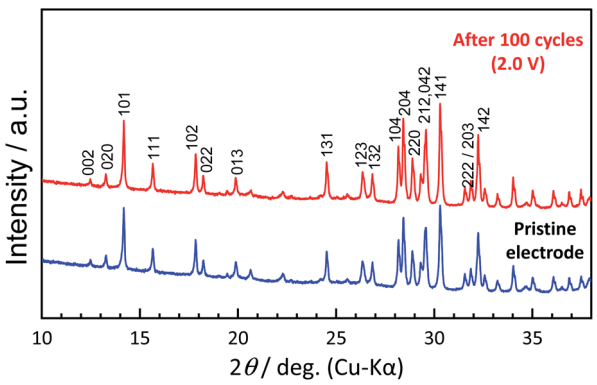

Fig. 4 Comparison of XRD patterns of pristine KVPP electrode and the KVPP electrode in the discharged state at 2.0 V at the 100th cycle.

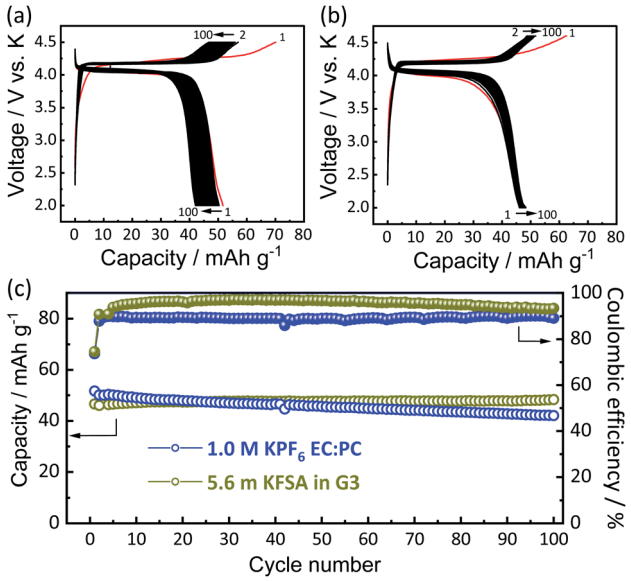

Fig. 5 Galvanostatic charge–discharge curves of KVPP electrodes in K cells filled with different electrolytes at C/20 rate in 2.0–4.5 V: (a) 1 mol dm^{-3} KPF_6/EC : PC (1 : 1 v/v) electrolyte and (b) 5.6 mol kg^{-1} KFSA/triglyme (G3) electrolyte. (c) Comparison of discharge capacity and coulombic efficiency of the two different electrolyte cells.

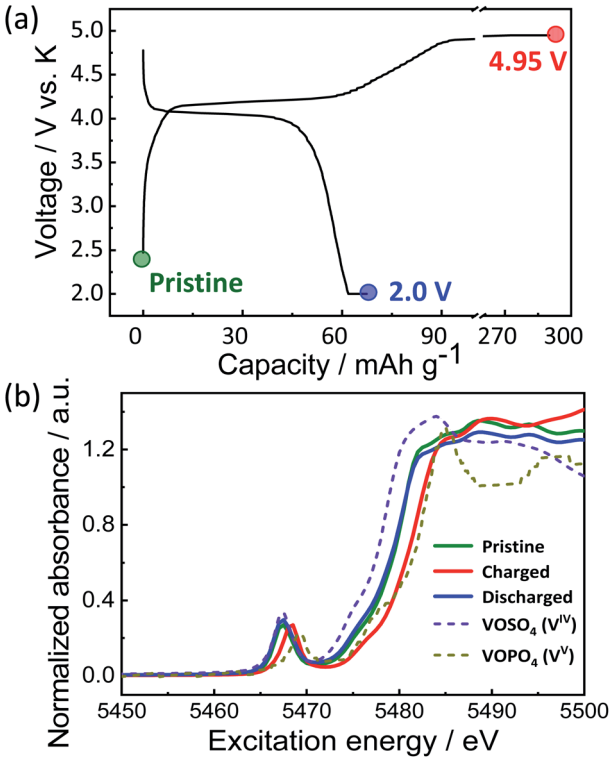

Fig. 6 (a) Voltage profile of KVPP electrode in a K cell and the points where *ex situ* XAS was conducted and (b) *ex situ* XANES spectra of the KVPP electrodes.

which suggest that the K insertion/extraction happens at a higher potential than Li and Na, agreeing with the difference of E^0 values of Li, Na, and K.[7] In the case of transition metal oxides like A_xCoO_2 (A = Li, Na, and K), the potassium analogues show the lowest working potential[6] while KVPP shows the highest working potential for potassium insertion.

To provide further insights into the charge compensation mechanism during K-extraction/insertion, hard X-ray absorption spectroscopy at vanadium K-edge was performed for the pristine material and the electrodes at the charged state (4.95 V) and the discharged state (2.0 V) as shown in Fig. 6a. As explained earlier, KVPP contains vanadium ions in the mixed valence states (V^{IV} and V^{V} states) which is confirmed from the X-ray absorption near edge structure (XANES) spectrum of the pristine material. The K-edge energy of all the pristine and charged and discharged electrodes falls between those of $VOSO_4$ (V^{IV} reference) and $VOPO_4$ (V^{V} reference) as shown in Fig. 6b, suggesting V^{IV} and V^{V} mixed state in $K_x(VO)_2(V_2O_3)_2(PO_4)_4(P_2O_7)$ during charging and discharging. During charging, oxidation of vanadium ions upon K extraction is evident from the shift in K-edge energy towards the higher energy of the $VOPO_4$ reference. Furthermore, the K-edge energy was lower in the discharged state (2.0 V) proving the reduction of vanadium ions. In addition, the spectrum of the KVPP electrode after discharging to 2.0 V matches exactly with that of the pristine material, indicating the structural reversibility and nearly complete re-insertion of K^+ ions into the structure.

Structural evolution

To understand the structural evolution of KVPP during the K-extraction/insertion, *operando* XRD measurements were carried out in a 3-electrode cell with K metal as both reference and counter electrodes. The material was charged/discharged at a slow current rate of C/40, and the recorded XRD patterns during the cycling are shown as a heatmap in Fig. 7a. The corresponding charge–discharge profiles of the KVPP electrode for the first and second cycles are also shown in Fig. 7b. At the beginning of charging, a voltage-plateau-like region was observed for initial 20 hours, but no change in the XRD pattern of the initial phase (phase A) was confirmed in this region. This is probably due to side reactions such as decomposition of electrolyte, resulting in a large irreversible capacity. By further charging, a new phase (phase B) emerged which co-existed with phase A in the subsequent plateau region. This two-phase reaction was evidenced from the decrease in the intensities of phase A, namely, 132, 204 and 220 diffraction peaks observed at 2θ = 27.0, 28.6, and 29.0°, respectively. There was a simultaneous increase in the intensity of new peaks belonging to phase B at 27.3 and 28.8°. At the end of charge at 4.5 V, the partially depotassiated phase (phase B) was observed as the sole phase through the two-phase reaction during the charging process. During the initial discharge process, a two-phase reaction similar to that of the charging process was observed, supporting the reversible extraction and insertion of potassium from and into the structure of KVPP.

To further confirm the structure at the discharge state as well as the charged state, *ex situ* synchrotron XRD was conducted for the electrodes in the charged state (4.5 V) and the discharged

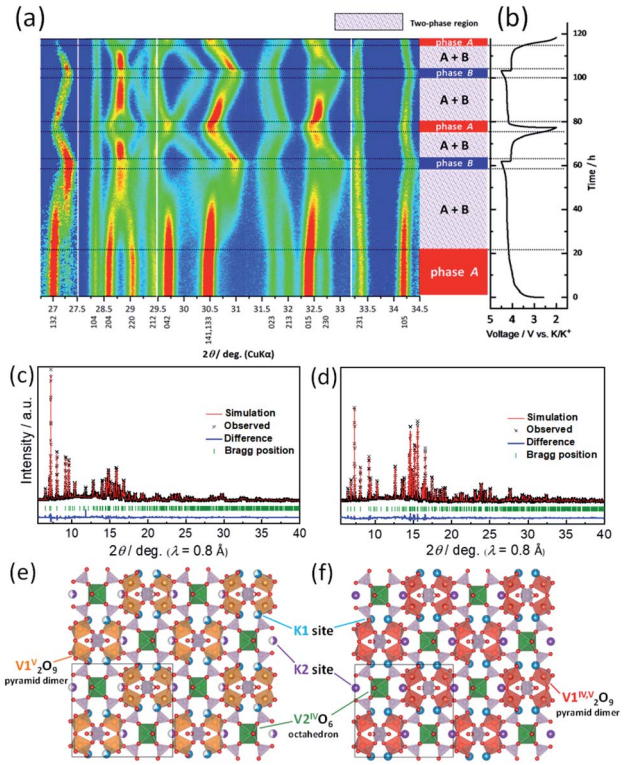

Fig. 7 (a) Contour map of *operando* XRD patterns in selected 2θ regions and identified phase regions. (b) Charge–discharge profiles during the *operando* XRD measurement. *Ex situ* synchrotron XRD patterns of the KVPP electrodes (c) charged to 4.5 V and (d) discharged to 2.0 V. (e and f) Refined crystal structures by Rietveld method for the XRD patterns shown in panel 'c' and 'd', respectively.

state (2.0 V). As shown in Fig. S8,† the XRD pattern of the charged state is different from the pristine material which is consistent with *operando* XRD data. Fig. 7c shows the Rietveld refinement XRD pattern of the charged KVPP electrode (Fig. 7e). The main diffraction peaks are consistent with those observed in the *operando* XRD as phase B and can be assigned to an orthorhombic lattice with *Pnma* space group with the following lattice parameters; a = 7.1372(2) Å, b = 13.0433(4) Å, and c = 14.1399(4) Å. The details of the refined structure of the charged state are shown in the Table S3.† The occupancy of the K1 and K2 sites (in Fig. 1b and c) was calculated from the refinement as 0.66 and 0.5, respectively. The refinement indicates that phase B has a formula of $K_{3.6}(VO)_2(V_2O_3)_2(PO_4)_4(P_2O_7)$, which is consistent with that estimated from the total current of the electrochemical data. After the first discharge, the synchrotron XRD pattern shows a similar pattern to that of the pristine KVPP, indicating that the material returns back to the pristine structure. Rietveld refinement was also carried out for the XRD pattern at the discharged state (Fig. 7d) and the crystal structure is shown in Fig. 7f. The refined parameters are shown in Table S4.† The occupancy of the K1 and K2 sites was calculated from the refinement as 0.98 and 1.0, respectively, indicating a complete re-insertion of K into the structure. Lattice parameters of the discharged state are calculated as a = 6.98358(12) Å, b = 13.3883(2) Å, and c = 14.2489(2) which are pretty close to those of the pristine electrode. These results suggest the excellent structural reversibility of KVPP upon charging and discharging. The structural refinement for the charged and discharged states reveals a small volume change of 1.2% during the charge/discharge process. Even considering the actual capacity, the volume change is very small compared to other potassium vanadium phosphate compounds, such as KTiOPO$_4$-type KVOPO$_4$ (3.3% for 84 mA h g^{-1})[20] and layered KVOPO$_4$ (9.4% for 115 mA h g^{-1}).[26] The fact indicates that KVPP has a low-strain structural change. The phase change during the second cycle (shown in Fig. 7a) is identical to that of the first cycle, which is in agreement with the robustness of the structure inferred from the similar XRD pattern of the material after 100 cycles as discussed in Fig. 3.

Conclusions

Highly pure oxide-phosphate-pyrophosphate framework material, $K_6(VO)_2(V_2O_3)_2(PO_4)_4(P_2O_7)$ (KVPP) was synthesized *via* thermal decomposition of the oxalatophosphate precursor, $K_2[(VOHPO_4)_2(C_2O_4)]$. KVPP shows reversible potassium extraction/insertion with a discharge capacity of 59 mA h g^{-1} corresponding to extraction/insertion of 2.7 mol K at a single discharge voltage plateau at 4.0 V at room temperature. *Operando* XRD measurements reveal that KVPP exhibits reversible structural changes *via* a two-phase reaction mechanism. The structural refinements of the initial phase and the charged state (4.5 V) confirm the robustness of the structure with a small volume change of 1.2% resulting in good cycle stability.

Author contributions

M. Ohara, A. Katogi, and K. Chihara conducted the material synthesis and the structural and electrochemical characterization. H. Tomooki prepared highly concentrated electrolytes and assisted the electrochemical tests. M. Ohara, A. S. Hameed, and K. Kubota prepared the manuscript. S. Komaba supervised the project and co-wrote the manuscript. All the authors discussed the results and contributed to writing the manuscript.

Conflicts of interest

There are no conflicts to declare.

Acknowledgements

The authors are grateful to Dr Toshinari Ichihashi and Prof. Yasushi Idemoto in the Tokyo University of Science for TEM measurements. This study was partly supported by the MEXT program "ESICB" (No. JPMXP0112101003), the Japan Science and Technology Agency (JST) through A-STEP program (No. JPMJTS1611), and JSPS KAKENHI Grant Numbers JP16K14103, JP16H04225, JP18K14327, and JP20K05690. The synchrotron X-ray diffraction experiments were performed at the BL02B2 of SPring-8 with the approval of JASRI (Proposal No. 2019B1282). The synchrotron hard X-ray absorption experiments were performed at the BL-12C of the Photon Factory under the approval

of the Photon Factory Program Advisory Committee (Proposal No. 2016G099 and 2018G673).

References

1 J. B. Goodenough and K. S. Park, *J. Am. Chem. Soc.*, 2013, **135**, 1167–1176.
2 M. Armand and J. M. Tarascon, *Nature*, 2008, **451**, 652–657.
3 N. Kittner, F. Lill and D. M. Kammen, *Nat. Energy*, 2017, **2**(6), 17125.
4 C. Vaalma, D. Buchholz, M. Weil and S. Passerini, *Nat. Rev. Mater.*, 2018, **3**, 18013.
5 C. Delmas, *Adv. Energy Mater.*, 2018, **8**, 1703137.
6 K. Kubota, M. Dahbi, T. Hosaka, S. Kumakura and S. Komaba, *Chem. Rec.*, 2018, **18**, 459–479.
7 T. Hosaka, K. Kubota, A. S. Hameed and S. Komaba, *Chem. Rev.*, 2020, **120**, 6358–6466.
8 X. Min, J. Xiao, M. H. Fang, W. Wang, Y. J. Zhao, Y. G. Liu, A. M. Abdelkader, K. Xi, R. V. Kumar and Z. H. Huang, *Energy Environ. Sci.*, 2021, **14**, 2186–2243.
9 S. Komaba, T. Hasegawa, M. Dahbi and K. Kubota, *Electrochem. Commun.*, 2015, **60**, 172–175.
10 Z. L. Jian, W. Luo and X. L. Ji, *J. Am. Chem. Soc.*, 2015, **137**, 11566–11569.
11 W. Luo, J. Y. Wan, B. Ozdemir, W. Z. Bao, Y. N. Chen, J. Q. Dai, H. Lin, Y. Xu, F. Gu, V. Barone and L. B. Hu, *Nano Lett.*, 2015, **15**, 7671–7677.
12 X. Wu, Y. L. Chen, Z. Xing, C. W. K. Lam, S. S. Pang, W. Zhang and Z. C. Ju, *Adv. Energy Mater.*, 2019, **9**, 1900343.
13 C. L. Zhang, H. P. Zhao and Y. Lei, *Energy Environ. Mater.*, 2020, **3**, 105–120.
14 B. Wang, Y. Peng, F. Yuan, Q. Liu, L. Z. Sun, P. Zhang, Q. J. Wang, Z. J. Li and Y. M. A. Wu, *J. Power Sources*, 2021, **484**, 229244.
15 A. Manthiram, *Nat. Commun.*, 2020, **11**, 1550.
16 K. Kubota, S. Kumakura, Y. Yoda, K. Kuroki and S. Komaba, *Adv. Energy Mater.*, 2018, **8**, 1703415.
17 T. Hosaka, T. Shimamura, K. Kubota and S. Komaba, *Chem. Rec.*, 2019, **19**, 735–745.
18 N. A. Chernova, M. F. V. Hidalgo, C. Kaplan, K. Lee, I. Buyuker, C. Siu, B. H. Wen, J. Ding, M. Zuba, K. M. Wiaderek, I. D. Seymour, S. Britto, L. F. J. Piper, S. P. Ong, K. W. Chapman, C. P. Grey and M. S. Whittingham, *Adv. Energy Mater.*, 2020, 2002638.
19 S. S. Fedotov, A. S. Samarin and E. V. Antipov, *J. Power Sources*, 2020, **480**, 228840.
20 K. Chihara, A. Katogi, K. Kubota and S. Komaba, *Chem. Commun.*, 2017, **53**, 5208–5211.
21 H. Kim, D. H. Seo, M. Bianchini, R. J. Clement, H. Kim, J. C. Kim, Y. S. Tian, T. Shi, W. S. Yoon and G. Ceder, *Adv. Energy Mater.*, 2018, **8**, 1801591.
22 J. Y. Liao, Q. Hu, X. D. He, J. X. Mu, J. R. Wang and C. H. Chen, *J. Power Sources*, 2020, **451**, 227739.
23 J. M. Dong, J. Y. Liao, X. D. He, Q. Hu, Y. F. Yu and C. H. Chen, *Chem. Commun.*, 2020, **56**, 10050–10053.
24 S. S. Fedotov, N. D. Luchinin, D. A. Aksyonov, A. V. Morozov, S. V. Ryazantsev, M. Gaboardi, J. R. Plaisier, K. J. Stevenson, A. M. Abakumov and E. V. Antipov, *Nat. Commun.*, 2020, **11**(11), 1484.
25 J. Hyoung, J. W. Heo, M. S. Chae and S. T. Hong, *ChemSusChem*, 2019, **12**, 1069–1075.
26 J. Y. Liao, Q. Hu, B. Che, X. Ding, F. Chen and C. H. Chen, *J. Mater. Chem. A*, 2019, **7**, 15244–15251.
27 W. Ko, H. Park, J. H. Jo, Y. Lee, J. Kang, Y. H. Jung, T. Y. Jeon, S. T. Myung and J. Kim, *Nano Energy*, 2019, **66**, 104184.
28 A. S. Hameed, A. Katogi, K. Kubota and S. Komaba, *Adv. Energy Mater.*, 2019, **9**, 1902528.
29 A. Eftekhari, *J. Power Sources*, 2004, **126**, 221–228.
30 X. F. Bie, K. Kubota, T. Hosaka, K. Chihara and S. Komaba, *J. Mater. Chem. A*, 2017, **5**, 4325–4330.
31 L. G. Xue, Y. T. Li, H. C. Gao, W. D. Zhou, X. J. Lu, W. Kaveevivitchai, A. Manthiram and J. B. Goodenough, *J. Am. Chem. Soc.*, 2017, **139**, 2164–2167.
32 X. Y. Wu, Z. L. Jian, Z. F. Li and X. L. Ji, *Electrochem. Commun.*, 2017, **77**, 54–57.
33 S. Chong, J. Yang, L. Sun, S. Guo, Y. Liu and H. K. Liu, *ACS Nano*, 2020, **14**, 9807–9818.
34 L. Li, Z. Hu, Y. Lu, C. C. Wang, Q. Zhang, S. Zhao, J. Peng, K. Zhang, S. L. Chou and J. Chen, *Angew. Chem., Int. Ed.*, 2021, **60**, 13050–13056.
35 A. J. Zhou, W. J. Cheng, W. Wang, Q. Zhao, J. Xie, W. X. Zhang, H. C. Gao, L. G. Xue and J. Z. Li, *Adv. Energy Mater.*, 2021, **11**, 2000943.
36 A. K. Padhi, V. Manivannan and J. B. Goodenough, *J. Electrochem. Soc.*, 1998, **145**, 1518–1520.
37 H. Kim, I. Park, S. Lee, H. Kim, K. Y. Park, Y. U. Park, H. Kim, J. Kim, H. D. Lim, W. S. Yoon and K. Kang, *Chem. Mater.*, 2013, **25**, 3614–3622.
38 D. Geiger, P. Balasubramanian, M. Mancini, P. Axmann, M. Wohlfahrt-Mehrens and U. Kaiser, Investigation of the cathode material $Li_9V_3(P_2O_7)_3(PO_4)_2$ for Li-batteries using Cs-corrected HRTEM, *European Microscopy Congress 2016: Proceedings*, 2016.
39 M. Ohara, A. S. Hameed, K. Kubota, A. Katogi, K. Chihara and S. Komaba, *presented in part at the 6th International Conference on Sodium Batteries (ICNaB-2019)*, Naperville, IL, USA, November, 2019.
40 I. V. Tereshchenko, D. A. Aksyonov, A. Zhugayevych, E. V. Antipov and A. M. Abakumov, *Solid State Ionics*, 2020, **357**, 115468.
41 A. S. Hameed, M. V. Reddy, M. Nagarathinam, T. Runcevski, R. E. Dinnebier, S. Adams, B. V. R. Chowdari and J. J. Vittal, *Sci. Rep.*, 2015, **5**, 16270.
42 S. Kawaguchi, M. Takemoto, K. Osaka, E. Nishibori, C. Moriyoshi, Y. Kubota, Y. Kuroiwa and K. Sugimoto, *Rev. Sci. Instrum.*, 2017, **88**(9), 085111.
43 F. Izumi and K. Momma, *Solid State Phenom.*, 2007, **130**, 15–20.
44 K. Momma and F. Izumi, *J. Appl. Crystallogr.*, 2011, **44**, 1272–1276.
45 B. Ravel and M. Newville, *J. Synchrotron Radiat.*, 2005, **12**, 537–541.
46 T. Hosaka, S. Muratsubaki, K. Kubota, H. Onuma and S. Komaba, *J. Phys. Chem. Lett.*, 2019, **10**, 3296–3300.

47 A. Leclaire and B. Raveau, *J. Solid State Chem.*, 2006, **179**, 205–211.
48 M. Jansen, *Solid State Ionics*, 1997, **101–103**, 1–7.
49 E. Le Fur, B. de Villars, J. Tortelier and J. Y. Pivan, *Int. J. Inorg. Mater.*, 2001, **3**, 341–345.
50 L. Benhamada, A. Grandin, M. M. Borel, A. Leclaire and B. Raveau, *J. Solid State Chem.*, 1991, **94**, 274–280.
51 N. Xiao, W. D. McCulloch and Y. Y. Wu, *J. Am. Chem. Soc.*, 2017, **139**, 9475–9478.
52 T. Hosaka, K. Kubota, H. Kojima and S. Komaba, *Chem. Commun.*, 2018, **54**, 8387–8390.
53 R. D. Zhang, J. Z. Bao, Y. H. Wang and C. F. Sun, *Chem. Sci.*, 2018, **9**, 6193–6198.
54 L. Qin, N. Xiao, J. F. Zheng, Y. Lei, D. Y. Zhai and Y. Y. Wu, *Adv. Energy Mater.*, 2019, **9**, 1902618.
55 T. Mandai, K. Dokko and M. Watanabe, *Chem. Rec.*, 2019, **19**, 708–722.
56 T. Hosaka, T. Matsuyama, K. Kubota, R. Tatara and S. Komaba, *J. Mater. Chem. A*, 2020, **8**, 23766–23771.